Investigation of the Saturation Properties of Gyroamplifiers

DAVID GOLOMB, YEHUDA GOREN, AMIRAM RON, AND JAY L. HIRSHFIELD

Abstract—**The saturation properties of a TE_{0n} gyroamplifier are investigated using a particle in cell numerical code. The effect of beam velocity spread is analyzed. It is found that for velocity spread ≤ 5 percent the reduction in efficiency can be compensated by extending the interaction length. A numerical optimization of efficiency enhancement using a tapered magnetic field is demonstrated. A change in the saturation mechanism from phase trapping to thermalization using the suggested tapering is observed.**

I. Introduction

GYROTRON AMPLIFIERS are developing into practical industrial products mainly in electronic countermeasure systems and in plasma diagnostics [1]–[4]. Their advantage over classical microwave devices is in amplifying electromagnetic (em) waves at high frequencies and to very high power levels. To make use of the potential high efficiency of the gyroamplifier, its saturation properties must be investigated [5]–[8].

The purpose of the present article is to analyze numerically the saturation properties of the gyroamplifier using a particle in cell simulation code, written in the Eulerian coordinate system. The space and time analysis enables us to take into account the electron velocity spread and a complex geometrical configuration, unlike space analysis [7]. The electron beam is simulated by a few thousand particles. The beam velocity spread [6], [8], [9] is analyzed using a few partial currents, each with different perpendicular and parallel velocity. The RF field is treated as a single TE_{0n} mode. Its transverse dependence is assumed to be that of the empty waveguide. To reduce computer time the RF field is analyzed in a multiple time and space scale technique. In this analysis the em field is represented as a combination of a fast oscillating term and a complex amplitude which varies on a slower time and space scale. The variation of the RF amplitude with time and space is solved self-consistently with the electron beam. To reduce the accumulated numerical errors the conservation of the total energy of the electron beam and the RF field is enforced along the axial direction every few wave periods. Our analysis enables us to make calculation with relatively short computation time compared to direct simulation [6]. Gyroamplifiers with long waveguide can be simulated and the dependence of the efficiency at saturation and the interaction length needed for saturation versus frequency can be examined.

In Section II a detailed description of the mathematical model is presented. The saturation properties are analyzed numerically in Section III. Section IV is devoted to the numerical optimization of the power efficiency by tapering of the magnetic field. With our new tapering method the efficiency at saturation can be doubled.

Manuscript received June 8, 1987; revised December 7, 1987.

D. Golomb and Y. Goren are with Rafael, P.O. Box 2250, Haifa, Israel, and the Department of Physics, Israel Institute of Technology, 32000 Haifa, Israel.

A. Ron is with the Department of Physics, Israel Institute of Technology, 32000 Haifa, Israel.

J. L. Hirshfield is with the Racah Institute of Physics, Hebrew University, Jerusalem, Israel.

IEEE Log Number 8820433.

II. Model Description

In the present analysis, a tenuous hollow electron beam propagates along the axis of a cylindrical conductor of radius R_W, parallel to an external magnetic field $B_0\hat{e}_z$. Every electron rotates with Larmor radius r_l around its guiding center. The guiding centers are located on a circle with radius R_0. Fig. 1 illustrates the basic configuration of the model. The electron beam is tenuous enough to enable us to neglect space charge effects. A single-mode approximation with empty waveguide radial dependence is assumed. In the present analysis TE_{0n} is assumed. Extending the model to different TE_{mn} modes is straightforward but consumes computer time.

The TE_{0n} mode of the empty waveguide is

$$E_\theta = EJ_0'(\alpha_{0n}r)\sin(k_z z - \omega t) \tag{1}$$

$$B_r = \frac{-k_z c}{\omega} EJ_0'(\alpha_{0n}r)\sin(k_z z - \omega t) \tag{2}$$

$$B_z = \frac{\alpha_{0n} c}{\omega} EJ_0(\alpha_{0n}r)\cos(k_z z - \omega t) \tag{3}$$

where E_θ is the azimuthal electric field with amplitude E, and B_r and B_z are the radial and axial magnetic fields, respectively. J_0 is the Bessel function of order zero, χ_{0n} is the nth root of J_0' and $\alpha_{0n} = \chi_{0n}/R_W$. These TE_{0n} modes can be derived from a vector potential $\vec{A}$:

$$\vec{A} = A_\theta \hat{e}_\theta = -\frac{c}{\omega} EJ_0'(\alpha_{0n}r)\cos(k_z z - \omega t)\hat{e}_\theta. \tag{4}$$

In the presence of an electron beam the vector potential can be decomposed into radial and axial components, consistent with the RF radial dependence assumption:

$$A_\theta = \hat{A}_\theta(z,t)J_0'(\alpha_{0n}r). \tag{5}$$

0018-9480/88/0600-0934$01.00

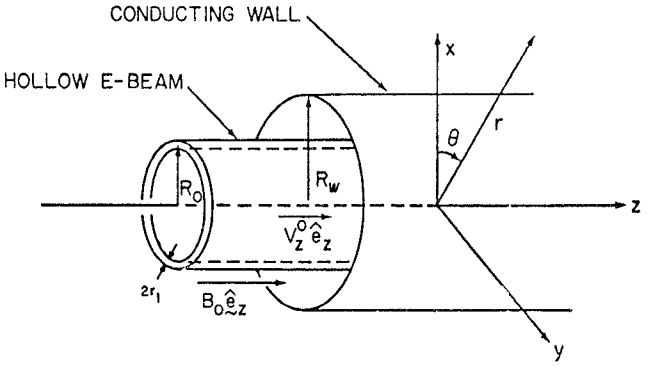

Fig. 1. Geometrical configuration. r_l is the Larmor radius.

Substituting (5) into Maxwell equations using the Lorentz gauge we obtain

$$J_0'(\alpha_{0n}r)\left[-\alpha_{0n}^2\hat{A}_\theta(z,t)+\frac{\partial^2\hat{A}_\theta}{\partial z^2}+\frac{1}{c^2}\frac{\partial^2\hat{A}_\theta}{\partial t^2}\right]=-\frac{4\pi}{c}J_\theta \tag{6}$$

where J_θ is the θ component of the electron current density $\vec{J}$. Multiplying (6) by $rJ_0'(\alpha_{0n}r)$ and integrating over r from 0 to R_W, the axial component of the vector potential $\hat{A}_\theta$ can be derived from

$$\frac{1}{c^2}\frac{\partial^2\hat{A}_\theta}{\partial t^2}-\frac{\partial^2\hat{A}_\theta}{\partial z^2}+\alpha_{0n}^2\hat{A}_\theta(z,t)=\frac{4\pi}{R_W^2G_{0n}c}\int_0^{R_W}rJ_\theta J_0'(\alpha_{0n}r)\,dr \tag{7}$$

where

$$G_{0n}=\int_0^1 xJ_0'^2(\chi_{0n}x)\,dx. \tag{8}$$

The electron current density in our simulation is represented by

$$J_\theta=-e\frac{Nl}{n_s}\sum_l v_\theta^l\frac{1}{r}\delta(r-r_l)\delta(\theta-\theta_l)\delta(z-z_l) \tag{9}$$

where the summation is over all the simulated charged particles n_s. N is the number of electrons per unit of length and l is the gyrotron length.

Transferring to dimensionless units where length is in units of R_W, time in units of R_W/c, and the vector potential in units of m_0c^2/e (m_0 is the electron's mass), (7) can be represented by

$$\frac{\partial^2\hat{A}_\theta}{\partial^2 t}-\frac{\partial^2\hat{A}\theta}{\partial^2 z}+\chi_{0n}^2\hat{A}_\theta=\frac{-4\pi\nu l}{G_{0n}n_s}\sum_l\beta_\theta^l J_0'(\chi_{0n}r_l)\delta(z-z_l)\delta(\theta-\theta_l) \tag{10}$$

where $\nu=Ne^2/m_0c^2$ is the Budker parameter and use has been made of the current density in (9), and $\beta_\theta^l=v_\theta^l/c$.

The physical problem of the RF amplification in low-current gyrotrons has two distinct spatial and temporal scales [8]: a fast oscillating traveling wave and a slowly varying amplitude. Making use of this assumption, the vector potential $\hat{A}_\theta$ can be decomposed as follows:

$$\hat{A}_\theta(z,t)=-\frac{1}{\omega}\,\mathrm{Re}\left[F(z,t)e^{i(k_zz-\omega t)}\right] \tag{11}$$

where ω and k_z are the temporal and spatial frequencies of the input wave. The backward wave in (11) has been neglected, because we assume perfect matching in the input and the output, and the beam current is below the threshold current for absolute instability [10]. We neglect second derivatives of F, consistent with the assumption of slowly varying amplitude.

$$\frac{\partial^2F}{\partial t^2}\ll\omega\frac{\partial F}{\partial t}$$
$$\frac{\partial^2F}{\partial z^2}\ll k_z\frac{\partial F}{\partial z}. \tag{12}$$

Substituting (11) into (10) and using (12), we obtain the amplitude equation:

$$i\left(\frac{\partial F}{\partial t}+\frac{k_z}{\omega}\frac{\partial F}{\partial z}\right)e^{i(k_zz-\omega t)}+\text{c.c.}=\frac{-4\pi\nu l}{G_{0n}n_s}\sum_l\beta_\theta^l J_0'(\chi_{0n}r_l)\delta(z-z_l)\delta(\theta-\theta_l) \tag{13}$$

where c.c. stands for complex conjugate. Multiplying (13) by $e^{-i(k_zz-\omega t)}$ and integrating over the time period $T=2\pi/\omega$ and the azimuthal angle θ, we obtain the final expression for the amplitude equation of motion:

$$\frac{\partial f}{\partial t}+\frac{k_z}{\omega}\frac{\partial f}{\partial z}=\frac{i\nu l}{G_{0n}n_s}\frac{\omega}{\pi E_0}\sum_l\int_{t-T}^{t}dt'\beta_\theta^l J_0'(\chi_{0n}r_l)\cdot\delta(z-z_l)e^{-i(k_zz-\omega t')}. \tag{14}$$

Here f is the normalized amplitude $f=F/E_0$, defined as the ratio of the RF amplitude to the input amplitude.

The effect of velocity spread is simulated in our model by several (5–7) partial currents I_p, each represented by n_{s_p} particles in the code. Each partial current has different axial and perpendicular velocities. When using this option (14) is replaced by

$$\frac{\partial f}{\partial t}+\frac{k_z}{\omega}\frac{\partial f}{\partial z}=\frac{iQ\omega}{\pi G_{0n}E_0}\sum_p\frac{I_pl}{ec\beta_{z_p}n_{s_p}}\sum_{l\in p}\int_{t-T}^{t}dt'\beta_\theta^l J_0'(\chi_{0n}r_l)\cdot\delta(z-z_l)e^{-i(k_zz-\omega t')} \tag{15}$$

where

$$Q=\frac{e^2}{m_0c^2R_W}. \tag{16}$$

The ratio between the partial current I_p with axial velocity β_{z_p} and the total current I is a Gaussian function of the form [8], [9]

$$\frac{I_p}{I}=K\delta(\gamma_p-\gamma_0)\exp\left[\frac{(\beta_{z_p}-\beta_{z_0})^2}{2(\Delta\beta_z)^2}\right] \tag{17}$$

where $m_0c^2\gamma_p$ is the energy of the electron that belongs to

the partial current I_p, β_{z_0} is the mean axial velocity, $\Delta\beta_z/\beta_{z_0}$ is the velocity spread, and K is a normalization constant.

Equation (15) is solved by finite differences. The mesh steps are Δz and Δt. The indexes n and j represent the time step and the z step accordingly. We obtain

$$f_j^{n+1} = f_j^m + \Delta t \cdot \left[-\frac{k_z}{\omega} \frac{f_j^n - f_{j-1}^n}{\Delta z} + \frac{iQ\omega}{\pi G_{0n} E_0} \cdot \sum_p \frac{I_p l}{ec\beta_{z_p} n_{s_p}} \sum_{i \in p} \int_{t-T}^{t} dt' \beta_\theta^i J_0'(\chi_{0n} r_i) \cdot \delta(z - z_i) e^{-i(k_z z - \omega t')} \right]. \quad (18)$$

In our simulation code the particle discreteness is replaced by a particle in cell with linear weighting.

The electron propagation (by the Lorentz force) is treated with a time-centered algorithm [11]. The phase error in the electron motion introduced by this algorithm is of order $(\Delta t)^3/3$, where Δt is the finite time step used. To improve the accuracy, the contribution to the phase change due to the external magnetic field has been replaced in the algorithm by the analytic expression every time step.

At the beginning, it is assumed that $f = 1$ along the waveguide and that the electrons are distributed according to (17). The boundary condition is that the field amplitude at $z = 0$ is equal to the input wave amplitude: $f = 1$. At $t = 0$ the interaction between the electrons and the em field is "turned on." Every time step the electrons are moved by the Lorentz force caused by the field and the field is changed according to (18) with the current position and velocity of the particles. The field amplitude f develops until it reaches steady state. In order to reduce accumulated numerical errors the total energy flow of the electrons and the RF field has been enforced along the gyrotron axial direction every few time periods of the wave.

The power of the em field is calculated by integrating the Poynting vector over the waveguide cross section and averaging the result over the time period of the wave. Since $f(z, t)$ is the ratio between the em amplitude at (z, t) and the em amplitude at the beginning, the power at z equals the power at the beginning multiplied by $|f|^2$. In terms of the em field amplitude at the beginning, E_0, the power is equal (in normalized units) to

$$P = \frac{k_z}{4\omega} G_{0n} E_0^2 |f|^2. \quad (19)$$

III. Numerical Results

The numerical analysis is done for the TE_{01} mode and the first cyclotron harmonic, in order to investigate the gyroamplifier's behavior at saturation. The beam and waveguide parameters were taken near the values usually used in gyrotron experiments [1]. The magnetic field chosen is $B_0 = 14$ kG, the conducting wall radius is 0.513 cm,

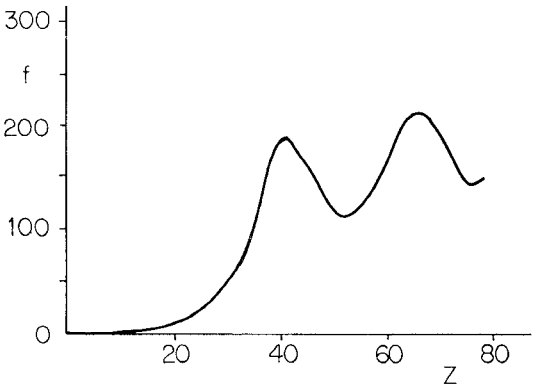

Fig. 2. The amplitude f versus z (in normalized units) in steady-state operation. $I = 2$ A, $\omega = 1.02\omega_g$, $B_0 = 14$ kG, $\beta_z = 0.25$, $\alpha = 1.6$, $R_W = 0.513$ cm, $R_0/R_W = 0.48$. The input power is 0.4 W.

$R_0/R_W = 0.48$, $\beta_{z_0} = 0.25$, and $\alpha = \beta_{\perp_0}/\beta_{z_0} = 1.6$. The electron's energy is 68.5 keV. A typical result for the case of 40 cm interaction length, 2 A electron current, and 0.4 W power input is shown in Fig. 2. The frequency is $\omega = 1.02\omega_g$, where ω_g is the grazing frequency determined by the tangential intersection of the electron and waveguide dispersion relations. In this example $\omega_g/2\pi = 36.83$ GHz and $\omega/2\pi = 37.57$ GHz. The curve shows the behavior of the microwave amplitude as a function of the axial distance along the interaction region. Three principal regions are observed: near the input port no microwave amplification is observed. At this stage the electron bunching is initiated. In the second region an exponential growth of the amplitude is observed corresponding to the stage of linear amplification. This stage is the stage described by the linear theories [5]. Very good agreement between our numerical results and these theories has been obtained. The third region is where the microwave amplitude reaches saturation. In this example the saturation mechanism is phase trapping [4] where the electrons are bunched and debunched periodically. This mechanism is represented in Fig. 2 by the spatial oscillation of the RF amplitude [5]–[7].

Saturation efficiency depends strongly on axial velocity spread. The reduction in efficiency can be partially compensated by applying longer interaction length to amplifiers with larger velocity spreads. In Fig. 3 we represent the amplitude amplification at saturation versus frequency (in units of grazing frequency ω_g) for an electron gun with 0 percent, 5 percent, and 10 percent velocity spread. The current is 1 A, $E_0/B_0 = 10^{-5}$ (in normalized units), and the other parameters are the same as above. It can be seen that from $0.98\omega_g$ to $1.02\omega_g$ the amplification is not reduced with velocity spread ≤ 5 percent. Note that the amplitude amplification reaches a maximum near the cutoff frequency $\omega_{co}/\omega_g = 0.968$, where the output power is reduced because of the low group velocity. The interaction length (units of wall radius R_W) versus frequency required for the above saturation condition is represented in Fig. 4. The length required is increased with frequency for all velocity spread initial conditions. Fig. 5 shows the output efficiency

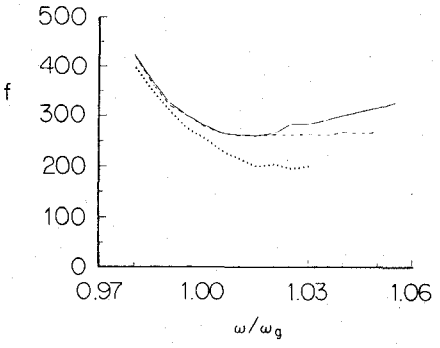

Fig. 3. Saturated amplitude versus frequency. $I=1$ A, $B_0=14$ kG, $\beta_z=0.25$, $\alpha=1.6$, $R_W=0.513$ cm, $R_0/R_W=0.48$. $E_0/B_0=10^{-5}$. The solid curve represents 0 velocity spread, the dashed curve 5 percent velocity spread, and the dotted curve 10 percent.

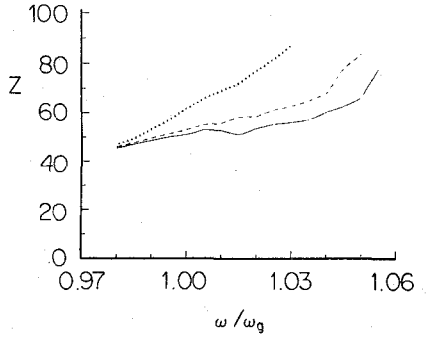

Fig. 4. Interaction length needed for saturation versus frequency. Parameters as in Fig. 3. The solid curve represents 0 velocity spread, the dashed curve 5 percent velocity spread and the dotted curve 10 percent.

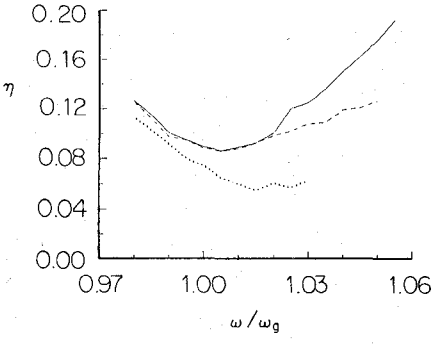

Fig. 5. Saturated efficiency η versus frequency. Parameters as in Fig. 3. The solid curve represents 0 velocity spread, the dashed curve 5 percent velocity spread and the dotted curve 10 percent.

versus frequency for the above parameters [6]. It can be seen that higher efficiency can be achieved for frequencies above the grazing condition, a result which is in contrast to the linear analysis, where the linear growth rate decreases with an increase in frequency. This nonlinear result is expected [4] since the average electron energy $\langle\gamma\rangle$ decreases because of the interaction with the em field. The dispersion relation curve of the electrons:

$$\omega = k_z v_z + \Omega_c/\langle\gamma\rangle \tag{20}$$

rises in the $\omega - k_z$ plane ($\Omega_c = eB_0/m_0c$). This causes its intersection with the waveguide dispersion curve to move to higher frequencies.

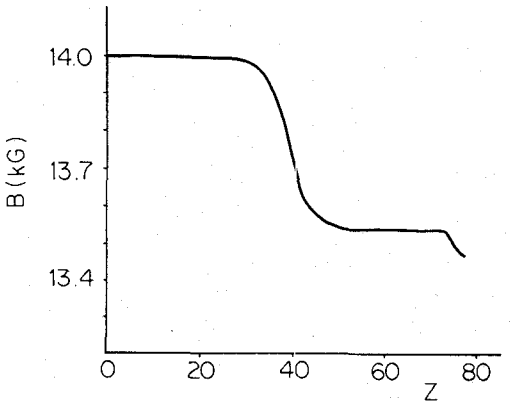

Fig. 6. Optimized magnetic field tapering for efficiency enhancement. $\omega=1.02\omega_g$.

At 5 percent axial velocity spread the saturation efficiency decreases for frequencies above $1.02\omega_g$. At 10 percent velocity spread the decrease is noticed at lower frequencies. Such decrease of the saturation efficiency with increase in the velocity spread was observed in rectangular geometries also [8]. Our numerical method enables us to calculate the efficiency of gyroamplifiers in circular configuration. However, it can be extended to other configurations.

IV. Magnetic Tapering

In the gyroamplifier with constant external magnetic field the phase trapping mechanism [5] is responsible for saturation. As the average energy $m_0c^2\langle\gamma(z)\rangle$ decreases, the electron dispersion curve is no longer tangent to the waveguide dispersion relation. To reduce the effect of this saturation mechanism we taper the magnetic field. The tapering is constructed so as to keep the relativistic cyclotron frequency constant along the axial direction:

$$\frac{\Omega_c(z)}{\langle\gamma(z)\rangle} = \frac{e}{m_0c}\cdot\frac{B_0(z)}{\langle\gamma(z)\rangle}. \tag{21}$$

In the ith iteration the average energy $\langle\gamma(z)\rangle_i$ as a function of z is calculated and a new magnetic tapering of the form

$$B_i(z) = B_{i-1}(z)\cdot\frac{\langle\gamma(z)\rangle_i}{\langle\gamma(z)\rangle_{i-1}} \tag{22}$$

is suggested for the next iteration. The final magnetic tapering is presented in Fig. 6 and the amplitude amplification for $\omega=1.02\omega_g$ is described in Fig. 7. From these figures it can be seen that the tapering is started at the final phase of the linear amplification stage. At this stage the electrons are giving an appreciable part of their energy to the RF field; therefore strong tapering must be applied to keep $\Omega_c/\langle\gamma(z)\rangle$ constant. Comparing Fig. 7 with Fig. 2, we can see an increase in the saturated amplitude by a factor of 1.45, which is a doubling of the gyroamplifier efficiency.

The effect of the tapering on the saturation mechanism can be seen from the behavior of the saturated amplitude

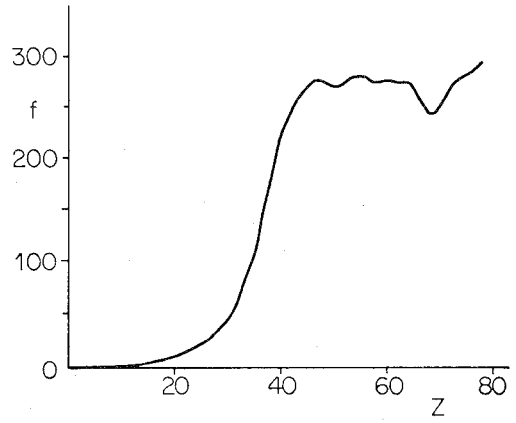

Fig. 7. The amplitude f versus z (in normalized units) in steady-state operation with the tapered magnetic field described in Fig. 6. Parameters as in Fig. 2.

as a function of z. As seen in Fig. 7, the microwave amplitude reaches a constant saturation level with almost no oscillations, contrary to the behavior in a constant magnetic field (Fig. 2). The phase trapping mechanism responsible for saturation in the constant magnetic field gyrotron is replaced by a perpendicular energy spread mechanism.

V. Conclusions

In this paper we investigated numerically the saturation properties of the gyroamplifier. The analysis is carried out using a particle in cell numerical code, for a tenuous hollow electron beam propagating down the axis of a smooth bore waveguide. It is assumed that the electrons interact with a single TE_{0n} mode, whose transverse dependence is assumed to be that of the empty waveguide. Two main directions are taken in the analysis: the effect of velocity spread on the saturation properties and the efficiency enhancement using a tapered external magnetic field. A very important feature of the velocity spread analysis is that reduction in efficiency due to velocity spread $\leqslant 5$ percent can be compensated by extending the interaction length. The length that is needed to reach saturation depends on the frequency.

In the efficiency enhancement analysis it is found that using our numerical technique for magnetic tapering, a factor of two in overall efficiency can be achieved.

References

[1] R. S. Symons and H. R. Jory, "Cyclotron resonance devices," in *Advances in Electronics and Electron Physics*, vol. 55. New York: Academic Press, 1981, pp. 1–75.

[2] V. L. Granatstein and S. Y. Park, "Survey of recent gyrotron developments," in *IEDM Tech. Dig.*, 1983, pp. 263–266.

[3] K. R. Chu, A. T. Drobot, V. L. Granatstein, and J. L. Seftor, "Characteristics and optimum operating parameters of a gyrotron traveling wave amplifier," *IEEE Trans. Microwave Theory Tech.*, vol. MTT-27, pp. 178–187, Feb. 1979.

[4] P. Sprangle and A. T. Drobot, "The linear and self-consistent nonlinear theory of the electron cyclotron maser instability," *IEEE Trans. Microwave Theory Tech.*, vol. MTT-25, pp. 528–544, June 1977.

[5] K. R. Chu, A. T. Drobot, H. H. Szu, and P. Sprangle, "Theory and simulation of the gyrotron traveling wave amplifier operating at cyclotron harmonics," *IEEE Trans. Microwave Theory Tech.*, vol. MTT-28, pp. 313–317, Apr. 1980.

[6] M. Caplan, A. T. Lin, and K. R. Chu, "A study of the saturated output of a TE_{01} gyrotron using an electromagnetic finite size particle code," *Int. J. Electron.*, vol. 53, pp. 659–671, Dec. 1982.

[7] Z. G. Chen, "Self-consistent large-signal calculation of the gyrotron-TWT," *Int. J. Infrared and Millimeter Waves*, vol. 5, pp. 73–89, 1984.

[8] A. K. Ganguly and S. Ahn, "Self-consistent large signal theory of the gyrotron travelling wave amplifier," *Int. J. Electron.*, vol. 53, pp. 641–658, Dec. 1982.

[9] Y. Y. Lau, K. R. Chu, L. Barnett, and V. L. Granatstein, "Gyrotron travelling wave amplifier: II. Effects of velocity spread and wall resistivity," *Int. J. Infrared and Millimeter Waves*, vol. 2, pp. 395–413, 1981.

[10] Y. Y. Lau, K. R. Chu, L. Barnett, and V. L. Granatstein, "Gyrotron travelling wave amplifier: I. Analysis of oscillations," *Int. J. Infrared and Millimeter Waves*, vol. 2, pp. 373–393, 1981.

[11] J. M. Dawson, "Particle simulation of plasmas," *Rev. Mod. Phys.*, vol. 55, pp. 403–447, Apr. 1983.

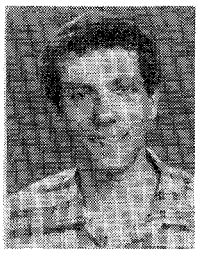

David Golomb was born in Tel-Aviv, Israel, in 1962. He received the B.Sc. degree in physics and mathematics from the Hebrew University in Jerusalem in 1983, and the M.Sc. degree in physics from the Technion—Israel Institute of Technology in 1986. During the years 1983–1986, he was with Rafael, Haifa, where he dealt with gyrotrons and plasma physics. Since 1987, he has been with the Israel Air-Force Testing Range.

Yehuda Goren, photograph and biography not available at the time of publication.

Amiram Ron, photograph and biography not available at the time of publication.

Jay L. Hirshfield, photograph and biography not available at the time of publication.